Frost halos from supercooled water droplets

Stefan Jung[a,b], Manish K. Tiwari[a], and Dimos Poulikakos[a,1]

[a]Laboratory of Thermodynamics in Emerging Technologies, Mechanical and Process Engineering Department, Eidgenössische Technische Hochschule Zürich, 8092 Zurich, Switzerland; and [b]European Aeronautic Defence and Space Company (EADS), EADS Innovation works, Department of IW-MS, 81663 Munich, Germany

Edited by William R. Schowalter, Princeton University, Princeton, NJ, and approved August 16, 2012 (received for review April 13, 2012)

Water freezing on solid surfaces is ubiquitous in nature. Even though icing/frosting impairs the performance and safety in many processes, its mechanism remains inadequately understood. Changing atmospheric conditions, surface properties, the complexity of icing physics, and the unorthodox behavior of water are the primary factors that make icing and frost formation intriguing and difficult to predict. In addition to its unquestioned scientific and practical importance, unraveling the frosting mechanism under different conditions is a prerequisite to develop "icephobic" surfaces, which may avoid ice formation and contamination. In this work we demonstrate that evaporation from a freezing supercooled sessile droplet, which starts explosively due to the sudden latent heat released upon recalescent freezing, generates a condensation halo around the droplet, which crystallizes and drastically affects the surface behavior. The process involves simultaneous multiple phase transitions and may also spread icing by initiating sequential freezing of neighboring droplets in the form of a domino effect and frost propagation. Experiments under controlled humidity conditions using substrates differing up to three orders of magnitude in thermal conductivity establish that a delicate balance between heat diffusion and vapor transport determines the final expanse of the frozen condensate halo, which, in turn, controls frost formation and propagation.

droplet science | explosive evaporation | multiphase physics | phase change | condensate freezing

Due to its frequent occurrence in nature and in everyday societal and technological applications, freezing of supercooled water has been studied intensively for decades (1–6). Models that aim at describing and predicting ice nucleation, ice adhesion, the conditions for atmospheric icing, and icing scaling methods in the aviation industry are seriously hindered by the complexity of icing physics, the sometimes unorthodox behavior of water (7, 8) and the many intricacies related to wetting phenomena and water-surface interactions (9).

In the pursuit of understanding and avoiding undesirable water freezing on surfaces, research efforts have recently focused on developing so-called "icephobic" surfaces that could potentially retard/avoid ice formation and contamination (10, 11). Such works have also shed light on the crucial and sometimes unexpected role of environmental conditions—e.g., frost, humidity, and shearing gas flow on the formation and potential delaying of icing on solid surfaces (12, 13).

The effect of the surface free energy of the substrates on frosting has been extensively studied (14–17). Through these works, it is now known that frost typically forms either directly from the vapor phase through ablimation (ablimation frosting) or via water vapor condensation on subcooled solids that generates supercooled water droplets, which then freeze through nucleation (condensation frosting) (17). Due to its obvious relevance to the fundamentals of surface frosting, the investigation of freezing of supercooled droplets on surfaces offers a basic platform to understand related key phenomena. Freezing of sessile droplets on a surface starts with a probabilistic event and completes via two partly overlapping stages (2, 18–20). First, a very rapid, kinetically controlled recalescent crystal growth takes place, resulting in an ice-crystal scaffold in the partially solidified liquid (20). In the second stage, the remaining liquid in the interspace of this ice scaffold freezes isothermally at a rate one to several orders of magnitude slower, which is mainly controlled by the rate at which the heat released during freezing is conducted into the substrate and dissipated to the environment (18, 20). Here we demonstrate that the freezing process is associated with the partial, initially explosive evaporation of the liquid droplet, a phenomenon with remarkable implications on frost formation and propagation on a solid surface. Under dry conditions, the heat released during freezing leads to a significant evaporation of the remaining liquid. We show herein that the vapor subsequently condenses symmetrically on the substrate in the neighborhood of the liquid droplet and forms a condensate halo, which eventually freezes due to the cold ambient temperature. The complex behavior of this so-formed frost halo involves multiple phase transitions and could also initiate freezing of neighboring droplets through a domino effect, illustrating a clear mechanism of frost propagation which was experimentally validated through high-speed visualization of the freezing process. Using heat transfer analysis and a diffusive vapor transport model, the size of the condensate halo is computed, which is critical to predict the possible sequential freezing of droplet arrays. It is established that condensate halo size depends critically on the thermal conductivity of the substrates and the surrounding humidity. Three examples and extreme cases of freezing on insulating PMMA [poly(methylmethacrylate)], conductive copper, and titanium substrates are used to illustrate the effect. Overall, the results shed light on the mechanism of frost formation and icing on solid surfaces, and establish the presence of evaporation/condensation from supercooled freezing liquid to have a critical influence on the dynamics of frost formation and propagation.

Results and Discussion

Three different substrates—PMMA, polished titanium, and copper—were employed in this study due to their widely different thermal conductivity values (21), but similar wettability (contact angle approximately 72°). Fig. 1 captures the freezing of a supercooled droplet (−14.5 °C) on the PMMA surface investigated in the experimental chamber (humidity ϕ of 1.3%) described in *Methods* and clearly captures the evaporation from the freezing droplet, the condensation of the vapor as microdroplets, and the subsequent freezing of the condensate. In the following discussion, the original 5-μl supercooled droplets are also referred as "mother" droplets in order to clearly distinguish them from the condensate microdroplets. In fact, the droplet evaporation was initiated through a flash; an explosive vapor formation nearly coincident with the first recalescent freezing stage and continuing through the second slower stage. The resulting water vapor diffused radially outward from the droplet with a characteristic

Author contributions: S.J., M.K.T., and D.P. designed research; S.J. and M.K.T. performed research; S.J. and M.K.T. contributed new reagents/analytic tools; S.J., M.K.T., and D.P. analyzed data; and S.J., M.K.T., and D.P. wrote the paper.

The authors declare no conflict of interest.

This article is a PNAS Direct Submission.

[1]To whom correspondence should be addressed. E-mail: dimos.poulikakos@ethz.ch.

This article contains supporting information online at www.pnas.org/lookup/suppl/doi:10.1073/pnas.1206121109/-/DCSupplemental.

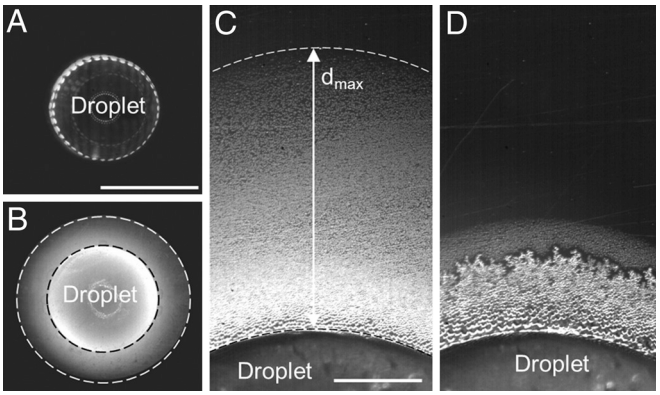

Fig. 1. Diffusion controlled evaporation and condensation halo around a freezing 5-μl droplet on PMMA. (*A*) An optical microscope image (top view) of a water droplet in a supercooled liquid state. (*B*) Diffusion controlled water condensation halo during freezing. The bright ring concentric to the droplet (area between white and black dashed circle) indicates the condensate region on the substrate. (*C*) Magnified segment of the condensate halo formed during droplet freezing. d_{max} indicates the maximal concentric expanse of the condensate halo. (*D*) Partial freezing of the condensate during its evaporation (dendritic ice morphology concentric to the droplet contact line). Scale bars for sequences (*A*) and (*B*) are 2 mm, and those for sequences (*C*) and (*D*) are 400 μm.

timescale of $\tau_D = l^2/D_v \approx 0.1$ s, where $D_v = 1.89 \times 10^{-5}$ m^2/s is the mass diffusivity of water vapor in air for a temperature of −14.5 °C (20) and l denotes a characteristic length, which can be taken as the droplet (volume 5 μl) diameter. Following the flash evaporation during recalescent freezing, the ambient gas in the vicinity of the mother droplet became supersaturated (saturation water vapor density at −14.5 °C is 1.65 g/m^3) and water condensed on the substrate in the neighborhood of the droplet. The partially condensed vapor field also formed a halo around the droplet. This explains the experimental observation shown in Fig. 1 and Movie S1.

The condensation from supersaturated gas occurs in the form of isolated supercooled micron-sized droplets, whose growth rate depends considerably on surface temperature and water contact angle (17, 20). In our experiments, dropwise condensation was observed immediately after the recalescent mother droplet freezing (Fig. 1*C*). During the second stage of mother droplet freezing, the situation began to change. Specifically, ice crystallization started at the droplet/substrate interface and moved upward. This motion led to a gradual reduction in the crystallization front area (correspondingly, the amount of latent heat released) as well as to a reduction of the unfrozen area from which water still evaporated (*SI Text*, *Role of substrate on droplet freezing*). As a result, the environmental conditions in the vicinity of the droplet switched gradually back from supersaturation to undersaturation and consequently the condensate on the substrate started to evaporate back to the environment (Fig. 1*D*). In addition, the condensate eventually also froze starting at the contact line of the mother droplet. We will show later that the frozen condensate can serve as ice nucleation initiator for any neighboring liquid, thereby playing an important role in frost formation and propagation. At this stage, we noted that the evaporation of the outer edge of the condensate halo occurred within the same time frame as the freezing of the same halo starting at the inner edge. The reason for this phenomenon will become clear after the analysis of vapor field, presented below.

The size of the condensate microdroplets gradually decreased with increased distance d from the mother droplet contact line (Fig. 1*C*), which is expected given the diffusive nature of water vapor transport through the gas and the sample surface characteristics (*SI Text*, *Critical supersaturation needed for condensation*). The salient features of the freezing process and the resulting condensate ring formed on various tested surfaces are summarized in Table 1. More details on condensate formation and size on tested surfaces are described in *SI Text*, *Evaluation of water condensation/evaporation*. Clearly the maximum condensate stretch on the more thermally conductive titanium and copper is considerably smaller due to a significantly faster mother droplet freezing on these surfaces (c.f., Table 1).

Table 1 also captures the role of the substrate thermal conductivity and ambient humidity in the formation of the condensate halo. The evaporation rate depends on the ambient humidity and the rate at which the latent heat released due to freezing is transmitted through the substrate (see *SI Text*, *Influence of humidity and substrate thermal conductivity on evaporation and condensation during freezing* for more details). With an increase in humidity, the maximum expanse of condensed water increased. This is because even though increased humidity reduced the evaporation rate, the surrounding gas was closer to the saturation state. On PMMA, growing microdroplets in the vicinity of the mother droplet eventually started coalescing in a manner similar to the coalescence observed in classical dropwise condensation in supersaturated environment (22). Finally, the condensate touched the frozen volume, initiating a rapid nucleation and freezing of microdroplets around the contact line (Fig. 1*D* and Movie S1). This phenomenon was not observed on titanium and copper due to their higher thermal conductivity, which facilitates rapid conduction of the heat of fusion through the substrate. The substrate thermal conductivity effect is also reflected in the time needed for completion of the mother droplet freezing (see Table 1). The reduced freezing time on titanium and copper resulted in a reduction in water evaporation and, consequently, in less condensed water in the vicinity of the freezing droplet. As a result, the condensed microdroplets on titanium and copper reevaporated well before they could freeze. Clearly, a delicate balance of condensate formation and its freezing or reevaporation will affect freezing of any neighboring droplets and thereby frost formation and propagation. Therefore, in the following, we

Table 1. Summary of test conditions and the resulting condensate halo properties. The condensate did not freeze on thermally conducting titanium and copper substrates, and therefore the respective size of the frozen condensate halo is marked as NA (not applicable). The standard deviation is based on three to four measurements.

Substrate	Test conditions			Test outcomes		
	Substrate thermal conductivity (W/mK)	Substrate and experimental chamber temperature (°C)	Humidity (%)	Mother droplet freezing time (s)	Maximum size of condensate halo (mm)	Maximum size of frozen condensate halo (mm)
PMMA	0.19	−14.5 ± 0.5	1.3	41 ± 5	1.4 ± 0.1	0.5 ± 0.2
			35 ± 3		2.2 ± 0.1	0.7 ± 0.1
Polished titanium	21.9	−14.5 ± 0.5	1.3	8.8 ± 1.5	0.9 ± 0.1	NA
Polished copper	400	−14.5 ± 0.5	1.3	3.1 ± 0.4	0.54 ± 0.06	NA

analyze the evolution in vapor mass concentration ρ_v around a freezing droplet through vapor diffusion. Note that the effect of vapor diffusion from the liquid–gas interface to the ice–gas interface of freezing droplets is separately considered in *SI Text*, *Diffusion controlled ice crystal growth* and is found to play no significant role in the vapor concentration determination as discussed.

To a first degree of approximation, the vapor diffusion from the droplet can be considered axisymmetric. Following the flash evaporation process during recalescent stage, the bulk of liquid evaporation, at least on the insulating PMMA surface, takes place in the second, slower freezing stage in which the freezing front starts at the droplet substrate interface and moves upwards. This movement progressively reduces the area of evaporation on the droplet surface. For a droplet freezing on PMMA, the freezing time (τ_f approximately 41 s) is much larger than the vapor diffusion time (τ_D approximately 0.1 s). Therefore, the evaporation and vapor concentration redistribution around the droplet can be approximated as quasisteady with respect to the much slower freezing process. The time-dependent movement of the freezing front along with the resulting area of evaporation was obtained by processing the digitized images from a side view video recording of the droplet freezing. For every time step and area of evaporation, the vapor diffusion was modeled using the axisymmetric, steady Laplace equation $\nabla^2\rho_v = 0$. A detailed description of the numerical solution and the experimental freezing front captured by image processing is given in *SI Text*, *Role of substrate on droplet freezing* and *Numerical model for quasisteady vapor diffusion*. Note that although the evaporation was initiated explosively with the recalescent stage of freezing, the condensate formation began only in the second stage. This is because the time for recalescent freezing (approximately 20 ms as detected from high-speed videos of the freezing process) is less than τ_D (approximately 100 ms, see also *SI Text*, *Role of substrate on droplet freezing*). The time scale difference justifies the focus of vapor concentration analysis during the second freezing stage. The temperature measurement at 0.7 mm into the droplet confirms that the temperature there remains at 0 °C until the freezing front passes through this region, thus justifying the second freezing stage to be similar Stefan-type freezing with the liquid temperature maintained at the interface equilibrium temperature (23).

Fig. 2 shows the numerically calculated time- and distance-dependent contours of radial water vapor concentrations. At any location, if the concentration is above saturated level the vapor should condense. When the concentration again falls below the saturation level, we should expect condensate to begin reevaporating. The time for which the concentration remains above the saturation level will determine the condensate microdroplet size at a given location, which in turn should determine the time needed for their evaporation once the concentration falls below saturated level. The experimentally determined instantaneous locations of the outer edge of the condensate are plotted as blue triangles in Fig. 2. The position of the condensate edge crosses the saturation contour line at its maximum value of approximately 1.4 mm after approximately 4 s. After approximately 4 s the condensate edge starts to recede due to evaporation. Ideally, the maxima in condensate edge should coincide with the location where the saturated contour meets the distance axis (approximately 1.6 mm in Fig. 2). This slight underprediction by the model should be due to the delayed detection of the condensate in our experiments, which was based on the change in the intensity of the recorded image due to condensate formation. The last data point of the outer condensed water boundary in Fig. 2 (blue triangle at $t = 49$ s) indicates the meeting point of the advancing condensate freezing front moving outward and the receding condensate evaporation front moving inward (see Fig. 1*D*). The evolution of condensate position shown in Fig. 2 is in fact averaged over four different measurements. The change in vapor concentration, as predicted by the quasisteady vapor diffusion model, is

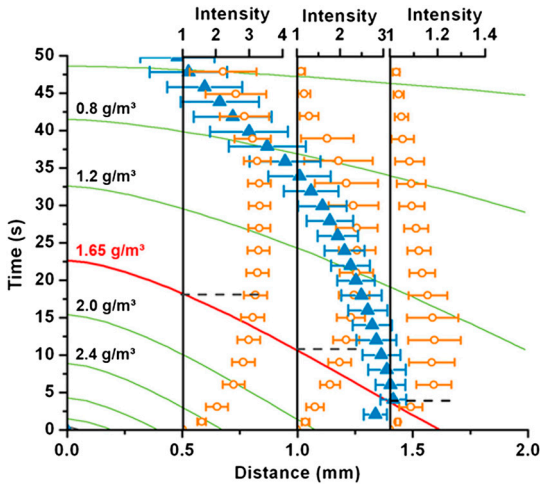

Fig. 2. Phase change around a freezing supercooled droplet on PMMA surface. The numerically computed contour plot of water vapor mass concentration (in g/m^3) variation at the substrate, along a radial line from the edge of the droplet (origin of the distance coordinate) due to evaporation are plotted as solid lines. The red contour line indicates the saturation concentration at −14.5 °C. The blue triangles indicate the outer boundary of water vapor condensation halo (experiment); i.e. the extent of the condensate. Topmost blue triangle marks the point at which the condensate is completely frozen. The orange circles show the locally averaged and normalized gray scale intensity values for three particular different distances (0.5 mm, 1.0 mm, and 1.4 mm) from the water droplet contact line. The intensities should correspond one to one with the size of the condensate microdroplets (see details in the text). The switching times (switch from supersaturation to undersaturation condition) for the three locations are indicated using horizontal dashed lines. The error bars reflect the standard deviation over four measurements.

clearly the reason for the condensate microdroplet nucleation, growth, and eventual evaporation from the outer edge of the condensate ring. However, the exact locations of condensate microdroplets around the mother droplet are inherently probabilistic. Therefore, the exact time at which a condensate microdroplet nearest to the freezing mother droplet touches it, and thereby starts the freezing of the condensate halo from the inner edge, varied to some extent. Notwithstanding the small variation in the exact initiation of the condensate freezing from inner edge and its evaporation from outer edge, in all our experiments with PMMA the two processes occurred within the same time frame and consistently overlapped in time.

The present quasisteady model can be utilized to predict the growth and evaporation of condensate droplets in the following manner. Due to a time-dependent variation of vapor concentration, the conditions for condensation observed in our experiments are markedly different from the classic condensation experiments (i.e., works on breath figures), where the experiments are performed by holding the vapor concentration constant (22). From simple geometrical optics, one can infer that the increase in local intensity of the images (Fig. 1 *C*–*D*) should be directly proportional to the size of the condensate droplets. To deduce the size evolution of condensed microdroplets at any distance from the mother droplet contact line, the average and normalized local intensities at any location were analyzed using an in-house developed program. Fig. 2 includes the normalized intensity variations at three locations. It is clear from these intensity evolutions that the microdroplets increase in size until the local vapor concentration switches from supersaturation to undersaturation (demarcated by the red contour line). Notice that the time at which the local intensity; i.e., average droplet size, maxima occurs is not inconsistent with the switch from supersaturated to undersaturated conditions. Thereafter, the normalized intensity values level off before deceasing to the value of the dry

substrate (the microdroplets completely evaporate) unless they freeze before they could completely evaporate, as shown in Fig. 1*D*. Contrary to an isolated, independently evaporating droplet (24, 25), droplets in closely packed agglomerates (as it is the case for the condensate on the surfaces in the present experiments) are known to evaporate in a cooperative manner by diffusive exchange of water vapor across each other and vertical diffusion into the environment (26, 27). In addition, since the curvature-dependent vapor pressure at the gas–liquid interface of a larger droplet is expected to be lower than on a neighboring smaller droplet [Kelvin equation (28)], the larger droplet should increase in size at the expense of the smaller one due to water vapor diffusion. This explains the averaged intensity values remaining almost constant for some time after reaching the maxima at locations 0.5 and 1.0 mm (see Fig. 2).

The freezing of droplet arrays was investigated next to exemplify the repercussions of the above findings on frost formation and propagation on surfaces. Fig. 3*A* shows the zoomed edges of two supercooled 5-μl droplets on PMMA with a separation of $d = 130$ μm. As explained earlier, after initial crystallization of the lower droplet in Fig. 3*B*, a condensing water front propagates towards the upper liquid droplet. The condensate also freezes starting near the edge of the lower droplet. The presence of the neighboring droplet, however, alters the conditions for condensation through diffusion-controlled condensation of water vapor upon it. In fact, due to this condensation on the neighboring water droplet (critical saturation condition at $\phi = 100\%$), the vapor concentration near it can fall below the critical value needed for condensation (i.e., critical saturation on PMMA >100% humidity) so as to avoid water condensation on the sample surface and resulting in a water- and ice-free zone. This explains the ice and condensate water-free gap near the dashed line in Fig. 3*B* (minimum gap size approximately 14 μm). The gap ensures that the freezing of the first droplet did not immediately initiate the freezing of the second droplet. However, for a sufficiently small droplet separation, this barrier is overcome by growing ice crystals, which are fed by surrounding water vapor through ablimation, triggering nucleation and consecutive freezing of the neighbor droplet (Fig. 3 *B*–*C*). This took 8.3 s for droplets in Fig. 3. The growth rate of such an ice crystal in this small gap strongly depends on the environmental humidity, the temperature, and the degree of water vapor supersaturation with respect to ice

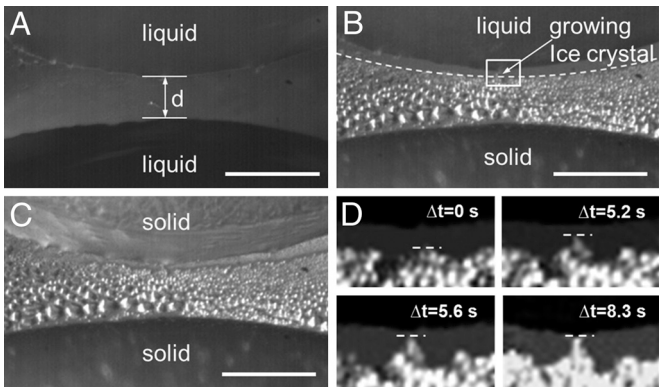

Fig. 3. Distance dependent nucleation by growing ice crystals. (*A*) Zoom in (top-view) on two liquid drops with a gap of width *d*. (*B*) Growth and freezing of condensate. The dashed line indicates the limit of condensate and marks the beginning of a water- and ice-free zone due to the reduced water vapor concentration in the vicinity of the upper (non-frozen) liquid water droplet (see *Results and Discussion*). (*C*) Upper droplet frozen through contact by the frozen condensate advancing from the bottom due to ablimation. (*D*) Snapshots of an ice crystal [magnified white box in (*B*)] growing for 8.3 s and crossing the water- and ice-free zone, thereby initiating freezing of the upper droplet. The horizontal dashed lines indicate the instantaneous outer edge of the growing crystal. The scale bar is 250 μm.

(20). In fact, 8.3 s was experimentally determined to be the time needed by an ice crystal at the edge of the frozen condensate to cross the water- and ice-free gap in Fig. 3 *B* and *D*. Considering the simple diffusive mass transport–driven growth of an ice crystal, in *SI Text*, *Diffusion controlled ice crystal growth* it is shown that such a crystal should grow following $a(t) \approx \sqrt{2\Gamma t + a_0^2}$, where a denotes the radius of the crystal, t the time, and subscript 0 the initial radius. The factor Γ depends on the degree of supersaturation S_I with respect to ice and other thermal parameters described in *SI Text*, *Diffusion controlled ice crystal growth*. Substituting the numerical values, it was found that a growth time of 8.3 s corresponds to an ambient humidity ϕ of $104 \pm 4\%$ in the gap between frozen condensate and the top droplet. This theoretical value is close to the critical saturation needed for water condensation on PMMA, as reported earlier (Fig. 2). It serves as an independent confirmation of the accuracy of vapor concentrations and the critical supersaturation needed for condensation.

The discussion above clearly establishes that, depending on the droplet separation and with strong enough evaporation and water condensation, frozen condensate is able to initiate nucleation in neighboring droplets resulting in a possible domino effect of independent water-droplet freezing over an entire droplet-populated surface (Movie S2), an interesting potential mechanism of frost propagation on solid surfaces.

Conclusions

Freezing of supercooled individual droplets and their arrays on solid surfaces were investigated both experimentally and theoretically to explore the mechanism of frost formation on solids. Three surfaces, with similar wettability but with thermal conductivity spanning a range of three orders of magnitude, were used in freezing tests at −14.5 °C. It was shown that droplet freezing is intimately associated with partial evaporation and subsequent condensation of the vapor forming a halo around the mother droplet. The droplet evaporation was initiated explosively by a recalescent, kinetically controlled freezing phase and progressed through a second, thermally controlled phase. The freezing time and thus the overall amount of evaporated water from the mother droplet was considerably higher on PMMA due to its low thermal conductivity.

The condensed microdroplets in the halo region could grow, coalesce, and eventually also begin to evaporate or freeze depending on the vapor concentration in their vicinity. The mother droplet evaporation and condensation in its neighborhood was explained using a quasisteady model capturing the vapor concentration profile in its vicinity. Image analysis was used to determine the local variation in the size of the condensate microdroplets. Eventually, the condensate microdroplets near the contact line came to contact with the freezing mother droplet and started to freeze. This initiated a sequential ice nucleation and freezing of condensate around the contact line, which resulted in a frost halo. The frost halo could interact with any neighboring sessile water droplet and, depending on its separation from the edge of the initial freezing droplet, initiate its crystallization. This frost propagation was also shown to be influenced by the rate of growth of frozen condensate microdroplets due to ablimation. A theoretical analysis presented to this end helped explain the experimentally measured time delay in frost propagation between two neighboring droplets (with a gap) in an array.

On more thermally conductive titanium and finally copper substrates under identical humidity and degree of supercooling, the condensate microdroplets evaporated completely before they could freeze due to the faster freezing of the mother droplet, thereby removing the source of liquid feed to the microdroplets. This clearly indicates that good thermal conductors may be effective in minimizing the frost propagation. In addition to the thermal conductivity, the substrate hydrophobicity, characterized by the contact angle and the associated hysteresis (12, 29), is an

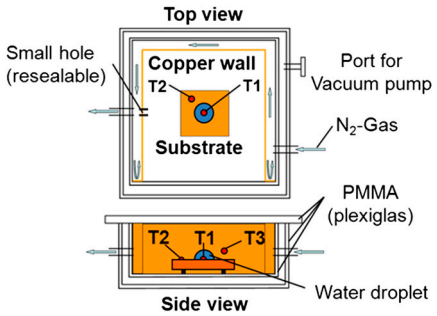

Fig. 4. Schematic of the experimental setup. Setup showing the location of the test sample, the water droplet inside the inner chamber, the surrounding flow of nitrogen gas (blue arrows) and thermocouples T1–T3 (red dots).

important parameter that influences liquid freezing on surfaces. The role of surface hydrophobicity in the evaporation-influenced freezing described herein, particularly in conjunction with the effect of substrate thermal conductivity variation, remains to be investigated.

The present findings demonstrate and explain the significant effect of the initially explosive evaporation and subsequent diffusion of water vapor from a freezing supercooled droplet on the frost formation and ice contamination process on a surface. The results shed light on frost propagation on solids in undersaturated environments and also highlight the crucial role of the substrate thermal conductivity in this regard. In addition to the clear impact on advancing the fundamental understanding of frost formation and propagation on surfaces, the study should have important consequences for various natural and technological applications, such as developing optimal icephobic surfaces.

Methods

Sample Surfaces. Smooth copper, titanium, and PMMA surfaces were used as substrates in the tests. The three choices were deliberate, since these three surfaces have similar wettability, but their thermal conductivity difference spans three orders of magnitude (21). The reported thermal conductivity values are 400 W/(mK), 21.9 W/(mK), and 0.19 W/(mK) for copper, titanium, and PMMA, respectively. The copper and titanium surfaces (30 mm × 30 mm × 2 mm) were polished using colloidal silica (OP-S, Struers), with an average grain size of 0.04 μm and a pH of 9.8, in order to reduce its surface roughness and match its morphology as closely as possible with the smooth PMMA sample (30 mm × 30 mm × 2 mm). The surface roughness R_a (arithmetic average) and the static water contact angle θ for polished copper, titanium, and PMMA surfaces were measured to be 0.024 ± 0.018 μm, $70 \pm 2°$; 0.036 ± 0.021 μm, $72 \pm 2°$ and 0.012 ± 0.007 μm, $73 \pm 3°$, respectively. The contact angle was measured using 5-μl deionized water droplets in a drop shape analysis setup (Kruess G10/DSA10). The roughness measurements were carried out using a confocal laser-scanning microscope (LSM, Olympus Lext OLS 3100). Each contact angle measurement was repeated five times on five different locations on each sample plate at room temperature of 22 °C and relative humidity of 40%.

Experimental Procedure and Apparatus. The experiments were performed in a double wall plexiglass chamber with inner dimensions 7 cm × 7 cm × 3 cm, and wall thickness of 8 mm as shown in Fig. 4.

A cryogenic cooler (KGW-Isotherm TG-LKF), generating a cold nitrogen vapor flow, was used to control the chamber temperature. A U-shaped copper wall (fitted into the inner chamber) was used to avoid the direct flow of cold nitrogen gas on to the sample surface located in the middle of the test chamber by diverting it along the inner wall of the chamber (Fig. 4). A vacuum pump connected to the plexiglass interspace evacuated the air in between the inner and outer walls of the chamber. This minimized the heat loss during experiments and helped avoid water condensation on the outer wall, which could interfere with the visualization of the droplet freezing process. No condensation of water vapor took place in the test section because the air, initially present in the test section, was eventually displaced by nitrogen gas through a small hole in the copper wall (Fig. 4). Without any additional endeavor to control the humidity, at steady state the humidity ϕ near the sample surface was measured to be $1.3\% \pm 0.3\%$ by using a humidity sensor (Graphtec humidity sensor, B-530). For running additional tests with increased humidity the nozzle of a piezo-electric nebulizer (with a flow rate of 500 mg/ min and a median droplet size of <4μ*m* diameter) was connected to the inner chamber of the setup to control the relative humidity value. In order to adjust the humidity, a precisely calculated (using psychrometric analysis for saturation at chamber temperature of −14.5 °C) amount of water from the reservoir of the nebulizer was gradually injected into the chamber volume (147 cm^3) until the humidity of nitrogen gas reached equilibrium.

Three T-type thermocouples (T1–T3 in Fig. 4) were used to continuously monitor the characteristic temperatures during the experiments. The sample substrate, monitored by T2, was cooled by the cold nitrogen gas. The temperature of the droplet ambient (monitored by T3) served as a feedback to the cryogenic cooler. The controller set point was −15 °C. After reaching steady state, the resulting equilibrated temperatures T2 and T3 were measured to be $-14.5\,°C \pm 0.5\,°C$. A 5-μl water droplet was inserted into the chamber through a resealable opening in the plexiglass chamber and cooled down to the ambient temperature by letting the droplet hang from the pipette at approximately 1 cm from the test sample before depositing it on the surface. A plastic pipette was used to introduce the droplet (13). Premature ice nucleation of the liquid volume could be avoided at with temperatures ≥ − 15 °C. A small drilled hole in each of the substrates was used to insert the T1 (0.08 mm diameter wires), which protruded up to approximately 0.7 mm from the surface and monitored the temperature of the sessile water droplet with a sampling rate of 10 Hz. The waiting time required for the droplet to reach ambient temperature was estimated using a sphericosymmetric diffusive heat loss from the pendant droplet initially at room temperature to the ambient of the experimental chamber (13). The estimated time was 13 s.

Due to the transparency of the plexiglass chamber, visual access was possible to the freezing droplet(s) both from the top and the side wall using a high-speed camera (Photron Fastcam PCI1024) mounted on a binocular microscope (Olympus SZ1145TR). The illumination for imaging was provided by a ring-like LED array fitted around the objective.

Experimental Data Evaluation. The condensation, evaporation, and crystallization mechanisms of supercooled water droplets were extracted by image processing using an in-house developed program in the software Matlab®. The essential approach used to analyze the size evolution of condensing and evaporating condensate water droplets is as follows. First, the high-speed video recording of the freezing process was digitized and converted into an image sequence. Then, in each image, a concentric condensate region was divided into radial sectors with an opening angle of 10°. The width of each sector was 20 pixels (approximately 55 μm). The average pixel (gray scale) intensity for any sector at any given time (represented by a particular image in a digitized image sequence), was normalized using the corresponding average intensity value for a dry surface prior to the beginning of the freezing process. The process was repeated for every image frame. The resulting time evolution of normalized intensity is plotted at three locations in Fig. 2. Since the freezing process was imaged in reflection mode, according to classic geometric optics, the image intensity in the regions covered with the condensate microdroplets should be characterized by reflection and scattering of light. In the case of a droplet surface the intensity at the apex (specular reflection) and the remainder of a droplet (reflection) should correlate with the droplet size for constant illumination conditions. This is because the droplet can be treated as a converging lens either reflecting the photons from the light source directly at its surface or absorbing and focusing the light at its apex. The larger the lens (droplet) the more photons can be directly reflected or absorbed and focused by the lens, resulting in higher intensity values for the measured pixels [the so-called increase in numerical aperture (30)].

1. Debenedetti PG (2003) Supercooled and glassy water. *J Phys Condens Matter* 15: R1669–R1726.
2. Hobbs PV (1974) *Ice Physics* (London, Oxford Univ Press).
3. Rosenfeld D, Woodley WL (2000) Deep convective clouds with sustained supercooled liquid water down to −375 °C. *Nature* 405:440–442.
4. Matsuoka S, Hibara A, Ueno M, Kitamori T (2006) Supercooled micro flows and application for asymmetric synthesis. *Lab Chip* 6:1236–1238.
5. Tabazadeh A, Djikaev YS, Reiss H (2002) Surface crystallization of supercooled water in clouds. *Proc Natl Acad Sci USA* 99:15873–15878.
6. Malkin TL, Murray BJ, Brukhno AV, Anwar J, Salzmann C (2012) Structure of ice crystallized from supercooled water. *Proc Natl Acad Sci USA* 109:1041–1045.
7. Ball P (1999) *H_2O: A Biography of Water* (Weidenfeld & Nicolson, London).
8. Mishima O, Stanley HE (1998) The relationship between liquid, supercooled and glassy water. *Nature* 396:329–335.
9. Quéré D, de Gennes P-G, Brochard-Wyart F, Reisinger A (2004) *Capillarity and Wetting Phenomena: Drops, Bubbles, Pearls, Waves* (Springer, New York).
10. Cao L, Jones AK, Sikka VK, Wu J, Gao D (2009) Anti-icing superhydrophobic coatings. *Langmuir* 25:12444–12448.

11. Mishchenko L, et al. (2010) Design of ice-free nanostructured surfaces based on repulsion of impacting water droplets. *ACS Nano* 4:7699–7707.
12. Varanasi KK, Deng T, Smith JD, Hsu M, Bhate N (2010) Frost formation and ice adhesion on superhydrophobic surfaces. *Appl Phys Lett* 97:234102.
13. Jung S, Tiwari MK, Doan NV, Poulikakos D (2012) Mechanism of supercooled droplet freezing on surfaces. *Nat Commun*, doi: 10.1038/ncomms1630.
14. Sahin AZ (1994) An experimental study on the initiation and growth of frost formation on a horizontal plate. *Exp Heat Tran* 7:101–119.
15. Lee H, Shin J, Ha S, Choi B, Lee J (2004) Frost formation on a plate with different surface hydrophilicity. *Int J Heat Mass Tran* 47:4881–4893.
16. Liu Z, Gou Y, Wang J, Cheng S (2008) Frost formation on a super-hydrophobic surface under natural convection conditions. *Int J Heat Mass Tran* 51:5975–5982.
17. Hoke JL, Georgiadis JG, Jacobi AM (2004) Effect of substrate wettability on frost properties. *J Thermophys Heat Tran* 18:228–235.
18. Davis SH (2001) *Theory of Solidification* (Cambridge Univ Press, Cambridge).
19. Feuillebois F, Lasek A, Creismeas P, Pigeonneau F, Szaniawski A (1995) Freezing of a supercooled liquid droplet. *J Colloid Interface Sci* 169:90–102.
20. Pruppacher H, Klett JD (1998) *Microphysics of Clouds and Precipitation* (Kluwer Academic Publishers, Dordrecht, Boston, London).
21. Lide DR, ed. (2007) *Handbook of Chemistry and Physics* (CRC, Boca Raton, FL).
22. Beysens D, Knobler CM (1986) Growth of breath figures. *Phys Rev Lett* 57:1433–1436.
23. Jiji LM (2009) *Heat Conduction* (Springer, Berlin, Heidelberg).
24. Hu H, Larson RG (2002) Evaporation of a sessile droplet on a substrate. *J Phys Chem B* 106:1334–1344.
25. Popov YO (2005) Evaporation deposition patterns: Spatial dimensions of the deposit. *Phys Rev E* 71:036313.
26. Lacasta AM, Sokolov IM, Sancho JM, Sagués F (1998) Competitive evaporation in arrays of droplets. *Phys Rev E* 57:6198–6201.
27. Schäfler C, Bechinger C, Rinn B, David C, Leiderer P (1999) Cooperative evaporation in ordered arrays of volatile droplets. *Phys Rev Lett* 83:5302–5305.
28. Israelachvili JN (1992) *Intermolecular and Surface Forces* (Academic, London).
29. Jung S, et al. (2011) Are superhydrophobic surfaces best for icephobicity? *Langmuir* 27:3059–3066.
30. Ippolito SB, Goldberg BB, Ünlü MS (2005) Theoretical analysis of numerical aperture increasing lens microscopy. *J Appl Phys* 97:053105.